Crystallinity Dependence of the Plasmon Resonant Raman Scattering by Anisotropic Gold Nanocrystals

Hervé Portalès,[†,‡,*] Nicolas Goubet,[†,‡] Lucien Saviot,[§] Peng Yang,[†,‡] Sergey Sirotkin,[⊥] Eugène Duval,[⊥] Alain Mermet,[⊥] and Marie-Paule Pileni[†,‡,*]

[†]Université Pierre et Marie Curie Paris 6, UMR 7070, LM2N, 4 place Jussieu, 75005 Paris, France, [‡]Centre National de la Recherche Scientifique, UMR 7070, LM2N, 4 place Jussieu, 75005 Paris, France, [§]Laboratoire Interdisciplinaire Carnot de Bourgogne, UMR 5209, Centre National de la Recherche Scientifique, Université de Bourgogne, 9 avenue A. Savary, BP 47870, 21078 Dijon Cedex, France, and [⊥]Laboratoire de Physico-Chimie des Matériaux Luminescents, Université Lyon1, UMR 5620, Centre National de la Recherche Scientifique, Bât. A. Kastler, 10 rue Ada Byron, 69622 Villeurbanne, France

Thanks to significant advances in the design and characterization of nanosized metal NCs with controlled morphology, the influence of their size, shape, and local environment on the surface plasmon resonance (SPR) is well established nowadays.[1−3] Understanding how such structural parameters can affect the NCs optical properties is of great interest since this sensitivity offers to be advantageously exploited for various sensing applications. In particular, one can mention the surface-enhanced Raman scattering (SERS) spectroscopy,[4] as well as the so-called localized surface plasmon resonance spectroscopy, which is demonstrated to be a powerful tool for sensing molecules of chemical and biological interest.[5] Although it is a common expectation that twins inside nanocrystals should influence the behavior of electrons, only rare studies have been dedicated to assess the effect of twinning defects on the properties of metal NCs.[6−8] At the current stage of the knowledge acquired from the latter results, the single-crystal particles are shown to exhibit superior sensing ability than polycrystalline ones, so that the physical properties of metal NCs could be tuned by controlling defects.[7,9] In parallel to this control, the proper characterization of the crystallinity in a large ensemble of NCs is therefore a potential significant issue, which still remains unaddressed. In this regard, low-frequency Raman scattering is a powerful technique to study the impact of crystallinity. The SPR-vibration coupling at the heart of the scattering process makes this technique sensitive to both NCs crystallinity and shape

ABSTRACT Au nanocrystals (NCs) with different crystalline structures and related morphologies are unselectively synthesized using an organometallic route. The acoustic vibrations of these NCs are studied by plasmon mediated low-frequency Raman scattering (LFRS). A splitting of the quadrupolar vibration mode is pointed out in the LFRS spectrum. Comparison of the measured frequencies with calculations and careful examination of the NCs morphologies by transmission electron microscopy ascertain this splitting as being an effect of crystallinity. The excitation dependence of the LFRS spectra is interpreted by the shape-selection of the NCs *via* plasmon—vibration coupling. These results give new insights into the crystallinity influence on both the vibrations of the NCs and their coupling with plasmons and demonstrate the relevance of elastic anisotropy in monodomain NCs.

through their impact on both the vibrations and the SPR.

Confinement of elastic waves inside nanosized crystalline particles drastically affects their vibrational behavior by inducing the discretization of the phonon density of states. The confined acoustic vibrations of isotropic spherical nanoparticles, for instance, can be classified according to the Lamb's model[10] as either torsional or spheroidal. Such vibrations of nanoobjects have been stimulating extensive research in the past few years to get a better knowledge of the specific vibrational properties of matter at the nanoscale. Various experimental techniques have been successfully used for their observation, such as low-frequency Raman scattering[4,11] (LFRS) and time-resolved pump—probe spectroscopy.[12,13] Studying noble metal nanoparticles by LFRS has been shown to be particularly useful because of the coupling of their vibrations to their dipolar SPR. Indeed, due to such a coupling, Raman scattering from the

vibrations of metal nanoparticles is mediated by their surface plasmons.[14] While the spheroidal modes characterized by the $l = 0$ and $l = 2$ angular momentum, which correspond respectively to pure radial and quadrupolar modes, are Raman active,[15] the quadrupolar modes correspond to the main feature of the LFRS spectra. A further consequence of the plasmon−vibration coupling lies in the fact that the Raman cross sections of the aforementioned active modes can be also highly sensitive on each parameter being able to modify the SPR energy, profile, or amplitude, like for instance, the nanoparticles size and shape or their local environment.[2,3,16]

Recently, it has been observed by LFRS experiments[17,18] and confirmed by calculations[19] that crystallinity of metal nanocrystals can significantly influence their acoustic vibrations in the case of a metal with high elastic anisotropy such as gold (Zener factor: 2.92). Using the resonant ultrasound (RUS) approach,[20] which is a standard numerical method suitable for the calculation of the vibrational frequencies of nanocrystals with anisotropic elasticity, Saviot et al.[19] have shown that the introduction of elastic anisotropy in the calculation of the frequencies dramatically lifts the degeneracy of most vibrational modes. In particular, for spherical monodomain Au NCs with cubic crystallinity, the 5-fold $l = 2$ quadrupolar mode splits into two different branches. Furthermore, by considering group theoretical arguments, the lower and upper branches, in increasing order of frequency, are found to be related to 2-fold and 3-fold degenerate modes, which are labeled with the E_g and T_{2g} irreducible representations, respectively (O_h point group).

Even though the influence of crystallinity on the NCs vibrations is theoretically predicted, it suffers from poor experimental investigations and, as mentioned above, only few papers have yet reported on the observation of such phenomenon.[7,9] This is mainly because synthesizing NCs with both a narrow size distribution and controlled crystallinity still remains a challenging issue nowadays. This lack may also be related to the limited capacity of time-resolved spectroscopy for observing the effect of crystallinity on the vibrations of nanoobjects since crystallinity weakly affects the radial breathing mode frequency, which is measured by this technique.[21]

In this paper, we report on the study by Raman scattering of the acoustic vibrations of Au NCs with different crystalline structures unselectively synthesized by using a one-step one-phase synthetic route.[22] The respective contributions of mono- and polycrystalline NCs to the Raman signal are pointed out. To properly assign the various features observed in the LFRS spectrum, the measured frequencies are compared with those calculated by using the RUS approach and the dependence of the Raman spectra on the excitation wavelength is also examined. These results clearly empha-

size the relevance of elastic anisotropy in nanosized crystals.

RESULTS AND DISCUSSION

Transmission electron microscopy (TEM) Characterization of the NCs Size and Crystallinity. Figure 1a,b shows both the bright field and conical dark field scan TEM images of the synthesized Au NCs. Using conical dark field TEM, we could identify the various crystalline structures making it therefore possible to estimate the respective amounts of monodomain NCs and their polycrystalline counterparts. Most of the nanocrystals shown in the TEM images exhibit inhomogeneous patterns, which clearly indicates their polycrystalline composition. Four typical patterns related to polycrystals are presented in Figure 1c. The first two examples correspond to patterns which are unambiguously assigned to the so-called multiply twinned particles[23] (MTPs), that is, a decahedron (image no. 1) and an icosahedron (image no. 2). Image no. 3 illustrates the case of a NC whose geometry is not precisely identified although several crystalline domains are distinguishable. In addition to NCs composed of multiple domains, like those described above, the occurrence of poorly twinned ones has also to be noted. For instance, some of them appear to be composed of only two crystalline domains joined by one single twin as for the NC shown in the image no. 4. In parallel, the TEM images also reveal the presence in quite a large amount of uniformly illuminated patterns (Figure 1d) that likely correspond to monodomain NCs, whose morphologies are assumed to be that of either a cuboctahedron or a truncated octahedron.[24] After analyzing the conical dark field scan TEM images over a total population of 2000 NCs, the amount of single crystalline particles is found to be approximately 30% of the full population. The major portion (~65%) is composed of MTPs and/or polycrystals, while 5% is poorly twinned nanocrystals. In spite of the large variety of NC structures present in our samples, the NCs size distribution is characterized by a very low polydispersity of around 6%. The size histogram is plotted in Figure 1e together with the corresponding fit by a Gaussian profile whose maximum is centered at $D_{max} = 5.3$ nm with a standard deviation $\sigma = 0.32$ nm. Other samples containing both Au MTPs and monodomain NCs in a quite similar amount but characterized by different size distributions have been prepared using the same route as the one described in the Experimental Methods section (see Figure S1 and the related text in the Supporting Information).

Relationship between Nanocrystal Shape and Crystallinity. As illustrated by the schemes and images presented in Figure 1c,d, the particle morphology directly depends on the atomic arrangement, so that NC shape and crys-
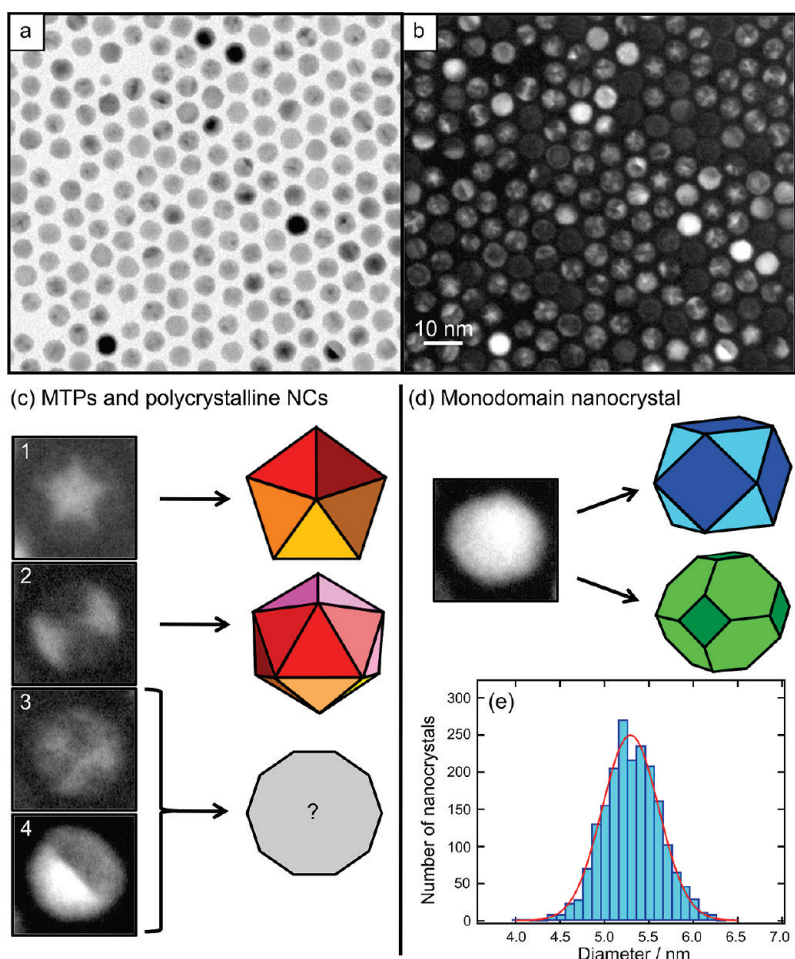
Figure 1. (a) Bright field and (b) conical dark field scan TEM images of Au NCs. (c) Zoom of few selected areas of the TEM images showing polycrystalline NCs with a schematic representation of the related shapes: (1) decahedron, (2) icosahedron, (3) polycrystal with undefined morphology and (4) single-twinned particle. (d) Same as previous for a monodomain NC whose typical morphology is found to vary from the cuboctahedron to the truncated octahedron. (e) Size histogram of the Au NCs determined by TEM analysis over 2000 entities. The maximum at D_{max} = 5.3 nm and the standard deviation σ = 0.32 nm of the NCs size distribution are deduced from its fitting by the Gaussian curve which is also plotted in the graph.

tallinity are two correlated structural parameters. For instance, the geometrical shape of monodomain Au NCs commonly varies from the cuboctahedron to the truncated octahedron,[24] and we will see in the following that these morphologies can be safely approximated by spheres for both calculating their SPR extinction spectrum and their vibrational frequencies. Besides, a large amount of polycrystalline NCs corresponds to MTPs with either quasi-spherical shapes, like icosahedra, or nonspherical ones, like decahedra.[23] Since the optical properties of nanoparticles are already shown to depend on their shape,[1−3] the following question arises here: Is the correlation between NC shape and crystallinity likely to enable the selective excitation of either single domain or polycrystalline NCs among a population of NCs with different crystallinities, in such a way to also permit the selective detection of their respective LFRS signal via plasmon−vibration coupling? As an attempt to address this problematic, the dependence of the SPR of Au NCs on their crystallinity-related shape and then, the influence of the anisotropic elasticity on

their acoustic vibrations will be successively considered below.

Dependence of the SPR of Au NCs on Their Crystallinity Related Shape. To investigate how the crystallinity might influence the SPR characteristics of the studied NCs via the change of their shape, extinction spectra have been calculated using the DDA method for the particular morphologies well identified from the TEM images that are shown in Figure 1a−c. To account for the presence of dodecanethiol molecules at the surface of the NCs, these latter are considered in the simulations to be immersed in a host medium with the same refractive index than the coating agent, that is, n = 1.46. All the calculated spectra are plotted in Figure 2 along with the UV−vis extinction spectrum measured from the colloidal solution used to elaborate our samples.

Except for the case of the decahedron, all the other calculated spectra exhibit nearly similar profiles where the intense band centered around 530 nm corresponding to the SPR of Au NCs is partially superimposed on its high-energy side to the onset of the interband tran-
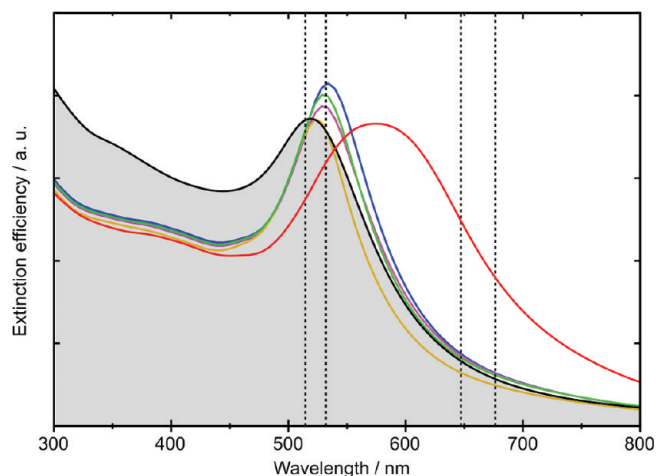
Figure 2. Experimental UV−vis extinction spectrum (filled black curve) of the colloidal Au solution plotted along with those calculated by using the DDA method for nanoparticles of different shapes: cuboctahedron (blue curve), icosahedron (violet curve), truncated octahedron (green curve), decahedron (red curve), and sphere (orange curve). The vertical dotted lines indicate the wavelengths of the various laser lines used as excitation sources for the LFRS experiments.

sitions. Furthermore, these spectra are found to be qualitatively in fairly good agreement with the experimental one, in which the SPR is peaked at around 520 nm. At variance, the spectrum calculated for decahedral particles shows the SPR band to be much broader and red-shifted with respect to those obtained for the other particle shapes. A recent study based on the spectroscopic measurements, imaging and modeling of individual Au decahedra pointed out their specific optical properties.[25] By comparing the various calculated spectra plotted in Figure 2, it is worth noting that the cuboctahedron, the truncated octahedron, and the icosahedron almost behave like spheres. The different optical behavior observed for the decahedron is due to its (oblate) shape anisotropy. In regard to this specificity, it should also be noted that the extinction spectrum calculated for the decahedral particles is orientationally averaged to account for their random orientation in the sample. The behavior of decahedral particles therefore enables the selective excitation of their SPR when turning the light wavelength from the green to the red in the Raman experiments. Despite a recent study of the effect of the lattice crystallinity on the electron−phonon relaxation rate in Au particles,[6] the actual influence of twins and other crystal defects on the characteristics of the SPR of nanosized NCs has not been yet precisely addressed to our knowledge. Unlike for the optical properties, we will examine here how the crystallinity can significantly influence the LFRS signal of Au NCs.

Effect of Crystallinity on the Acoustic Vibrations of Au NCs. As mentioned above, our previous study of the acoustic vibrations of Au NCs by LFRS[18] already permitted us to clearly demonstrate the specific vibrational behavior of quasi-spherical monodomain NCs, that arises from their anisotropic elasticity. Indeed, two bands were observed

in the LFRS spectrum of Au NCs whose frequencies were found to be in good agreement with those calculated by using the RUS approach for the E_g and T_{2g} modes of a so-called elastically anisotropic Au sphere,[18] that is, a sphere with internal cubic monodomain crystallinity. Additionally, one shoulder was also observed on the low-frequency side of the aforementioned T_{2g} band. This latter feature was ascribed to the usual $l = 2$ fundamental quadrupolar mode of NCs with imperfect crystallinity by describing their vibrations as those of a "fictive" elastically isotropic Au sphere, that is, a sphere with orientationally averaged elastic parameters of Au.

Like it is noticed for the SPR of Au NCs with spherical-like polyhedral morphologies (truncated octahedra, cuboctahedra or icosahedra), the vibrational frequencies were found to be almost unaffected by the shape variation between one morphology to the others and weakly deviate from the frequencies calculated for an Au sphere with the same volume.[18] At variance, considering the significant shape effect observed in Figure 2 on the SPR spectrum of the Au decahedron, it is important here to address the vibrations of this latter NC. The vibrational frequencies of the Au decahedron have been calculated by the RUS method using isotropic (i.e., orientationally averaged) elastic parameters of Au in order to account for the different orientations of the five tetrahedral crystalline domains making up each decahedron. The vibration modes have been labeled according to the irreducible representations of the D_{5h} point group. The low-frequency Raman active vibrations are reported in Table 1.

Unlike the case of MTPs with quasi-spherical shapes (icosahedra) that are characterized by one single quadrupolar mode, the decahedral morphology gives rise to (i) partial liftings of degeneracy of the quadrupolar mode and (ii) additional mixings of the previous modes with low-frequency modes affiliated with torsional type motions which are not Raman active for a sphere with isotropic elasticity. In the low-frequency range, three 2-fold degenerate E modes and one A mode are found to be Raman active and significantly contribute to the Raman spectrum for the decahedron. The spheroidal $l = 2$ vibrations of a sphere with isotropic elasticity are split into E'_2 (for $m = \pm2$), E''_1 (for $m = \pm1$) and A'_1 (for $m = 0$). Note that the E''_1 modes are further strongly mixed with torsional vibrations which are not Raman active for the sphere. This is the reason why E''_1 appears twice in Table 1. Taking into account a minimum bandwidth for each mode of around 20 GHz, as measured for the E_g mode of monodomain NCs, and due to the spectral distribution of the various modes, all of them lie in a narrow frequency range centered at a frequency which is close to that of the 5-fold quadrupolar modes of an isotropic sphere with the same volume. As a result, the contributions to the LFRS signal originating from icosahedra and decahedra are

TABLE 1. Comparison of the Vibrational Frequencies of 5.3 nm Au NCs Measured by LFRS with Those Calculated by Using the RUS Approach for Objects with Different Elastic Properties and Shapes

	objects used for modeling			frequencies (GHz)	
types of nanocrystal/crystallinity	elasticity	shape	modes	calculated[a]	measured[b]
cuboctahedron/MD truncated octahedron/MD	anisotropic	sphere	E_g	141	137 ± 10
			T_{2g}	227	210 ± 10
icosahedron/MTP	isotropic	sphere	$l = 2$	200	183 ± 10
decahedron/MTP	isotropic	decahedron	E'_2	167	
			E''_1	192	
			A'_1	202	
			E''_1	219	

[a]The 2-fold E_g and 3-fold T_{2g} degenerate modes of an Au sphere with anisotropic elasticity are considered for modeling the vibrations of monodomain (MD) NCs, like a cuboctahedron or a truncated octahedron. At variance, "fictive" elastically isotropic objects with spherical and decahedral shapes are used for simulating the $l = 2$ quadrupolar mode of an icosahedron and the Raman active modes of a decahedron, respectively, which are both multiply twinned particles (MTPs). In this last case, the frequencies are calculated for a decahedron with the same volume as the previous spheres. [b]The "measured" frequencies are averaged values derived from the LFRS measurements performed at various points of the sample and using four different excitation wavelengths.

both expected to identify with the band observed at around 183 GHz, so that it is not possible to distinguish between them solely on the basis of the measured Raman frequencies. As we will see now, the resonant Raman process with metal NCs does allow doing so.

Figure 3 shows the Stokes/anti-Stokes LFRS spectra of the deposited 5.3 nm Au NCs. All these spectra exhibit two dominant bands in the spectral domain below 250 GHz. Such a behavior has also been observed from other samples containing both Au MTPs and monodomain NCs with different size distributions, as illustrated by Figure S2 in the Supporting Information. This result is consistent with the observation of similar features in previous Raman experiments[18] that were performed by using an excitation at 532 nm on various samples containing monodomain Au NCs in a quite similar amount than those investigated in this work. The comparison of the measured vibrational frequencies with those calculated by using the RUS approach (Table 1) makes it possible to assign the various contributions coming out of the LFRS spectra displayed in Figure 3 in the following way: (i) the sharp band peaked at 137 ± 10 GHz is ascribed to the 2-fold degenerate E_g modes of monodomain Au NCs. (ii) The second band at higher frequency, which clearly appears to be broader than the former, also exhibits a structured profile, especially when looking at the spectrum recorded for an excitation wavelength of 676.4 nm. Actually, this band is originating from two different contributions to the Raman signal, that is, on the one hand, the Raman scattering from the 3-fold degenerate T_{2g} modes of monodomain NCs, corresponding to the peak centered at 210 ± 10 GHz, and on the other hand, the light scattering due to the "$l = 2$" vibrations of MTPs and polycrystalline NCs. From the calculated frequencies listed in Table 1, one can predict this last contribution to correspond to the shoulder that appears at around 180 GHz, on the low-frequency side of the T_{2g} band. To further argue in favor of the above assignation, it is important to consider that such a satisfactorily concordance

between measured and calculated vibrational frequencies is also confirmed for other samples of Au NCs with different size distributions (see Table S1 in the Supporting Information).

As shown in Figure 3, the profile of the LFRS spectrum depends on the excitation wavelength through the variation of the relative intensities of the three different contributions from one excitation to the others. Moreover, no shift of these components is observed when changing the excitation from the green to the red. This last result is noticeably in contrast with previous observations of plasmon-mediated Raman scattering from acoustic vibrations confined either in rough metal surfaces[4] or in matrix-embedded silver nanoparticles,[26] which clearly revealed a shift of the quadrupolar band toward lower frequency when shifting the excitation to larger wavelength. This feature was then demonstrated to reflect the presence of ellipsoidally distorted nanoparticles in the matrix together with spherical ones. Therefore, we can conclude that the invariance of the Raman bands positions when changing
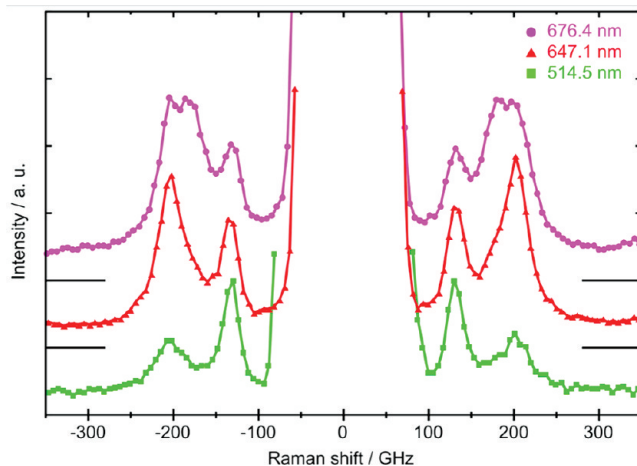

Figure 3. Stokes/anti-Stokes LFRS spectra of 5.3 nm Au NCs. The wavelengths of the different laser lines used as the excitation source are successively 514.5, 647.1, and 676.4 nm, from the bottom to the top. Spectra have been vertically shifted and amplitudes normalized to the maximum of the lowest frequency band for clarity.
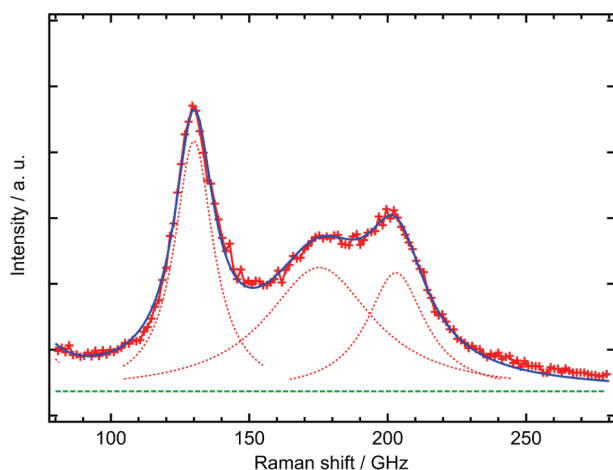
Figure 4. High-resolution Stokes LFRS spectrum of 5.3 nm Au NCs (red curve with crosses) recorded for an excitation at 532 nm. The entire profile of the spectrum is satisfactorily reproduced (blue curve) by ascribing to each component a Lorentzian profile (red dotted curves) represented along with the constant background (green dashed line) that is also involved in the multipeak fitting.

the laser wavelength results from the narrow shape and size distributions of the studied Au NCs, in agreement with the TEM image shown in Figure 1.

To support the assignment given above and more precisely define the origin of the various features in the multiple component LFRS signal measured from both monodomain and polycrystalline Au NCs, we show in Figure 4 one high-resolution Stokes LFRS spectrum. In this highly resolved spectrum, the three components, whose assignment is given above, are clearly distinguishable. To further characterize these various features and their respective dependence on the excitation wavelength, their intensities were derived from a multipeak fitting of the structured LFRS spectrum. As illustrated in Figure 4, the three-component profile is therefore successfully fitted by ascribing to each band a Lorentzian profile and by considering the additional contribution of a constant background. This latter contribution is limited to a few percents of the whole signal and could be assumed to account for the residual signal potentially arising from the substrate or some impurities present in the sample as well as the electronic noise inherent to the detection system.

Figure 4 shows that the $l = 2$ band is significantly broader than the E_g and T_{2g} bands. This feature can be easily understood when considering the various possible origins for the broadening of the Raman bands, and in particular the shape[19] and size[27] dispersions of the NCs as well as the presence of defects in their crystalline structure.[28] The discrepancy qualitatively observed between the width of the $l = 2$ band and that of the E_g and T_{2g} bands is therefore fully consistent with the assignment of the former band to polycrystalline NCs and MTPs, like icosahedra and decahedra. Indeed, as mentioned above, for these two latter types of NCs, various vibration modes are expected to be Raman active in the low-frequency range with a quite large dis-

persion of the related frequencies (Table 1). Moreover, the narrower bandwidth estimated for the E_g and T_{2g} bands well agrees with their assignment to monodomain NCs of quasi-spherical shapes, like cuboctahedra and truncated octahedra.

The accurate derivation of the integrated intensity of each individual band from such a multipeak fitting procedure, as the one shown in Figure 4, is difficult for most spectra due to the partial superimposition of the two higher frequency bands. Actually, the measurement of the LFRS signal with a so high resolution as that obtained for an excitation at 532 nm was not achievable for the other wavelengths, due to technical limitation, making therefore the individual band fitting less precise in these latter cases. Nevertheless, using this procedure made it possible to reliably estimate the integrated intensity of the E_g band, on the one hand, and that of the structured band corresponding to the additional contributions of the $l = 2$ and T_{2g} bands, on the other hand. To examine the evolution of the LFRS spectrum profile on the excitation wavelength, the ratio $R(\lambda)$ of the integrated intensity of the higher frequency structured band to that of the E_g band has been calculated. The ratios presented in Table 2 correspond to averaged values as derived from the fit of various LFRS spectra recorded at each wavelength.

As indicated in Table 2, the smallest value of the $R(\lambda)$ ratio is obtained for an excitation at 514.5 nm. This should reflect the predominant contribution of monodomain Au NCs in the scattering process at this wavelength, especially *via* their E_g vibrational modes, and likely argues in favor of a more efficient plasmon−vibration coupling for monodomain NCs than for MTPs.[28] Regarding the extinction spectra plotted in Figure 2, it appears that decahedra mainly absorb light *via* interband electronic transitions at 514.5 nm, which have been actually shown to not couple with the NCs vibrations, so inducing no enhancement of the Raman scattering.[29] The more efficient contribution of monodomain NCs to the LFRS signal at 514.5 nm can therefore result from the selective excitation *via* plasmon−vibration coupling of quasi-spherical NCs, while most of decahedral MTPs do not contribute to the scattering. When turning the excitation to 532 nm, the contribution of decahedra to the Raman scattering process significantly increases while other polycrystalline particles, like icosahedra, still remain resonantly excited and efficiently scatter the light. The significant increase of the $R(\lambda)$ ratio observed when changing the excitation from 514.5 to 532 nm is consistent with the increasing contribution of decahedra to the Raman signal. Whatever the excitation wavelength in the red is, 647.1 or 676.4 nm, the $R(\lambda)$ ratio almost remains unchanged, keeping the same value as the one determined at 532 nm. The contribution of quasi-spherical NCs to the LFRS signal is logically expected to progressively decrease when shifting the excitation to the red.

TABLE 2. Ratios at Four Different Wavelengths of the Integrated Intensity of the Raman Band Corresponding to the Additional Contributions of Both the Threefold T_{2g} Degenerate Modes of Monodomain Au NCs and the Low-Frequency Raman Active Modes of Au MTPs to the Integrated Intensity of the Band Ascribed to the Twofold E_g Modes of Monodomain Au NCs

wavelength	514.5 nm	532 nm	647.1 nm	676.4 nm
ratio $R(\lambda)$	1.4 ± 0.4	3.2 ± 1.1	3.0 ± 0.9	3.4 ± 0.6

As a matter of fact, the low extinction cross sections calculated for both cuboctahedra and truncated octahedra at 647.1 and 676.4 nm (Figure 2) makes it possible to predict the vanishing of the LFRS signal from monodomain NCs at these two last wavelengths. The invariance of the $R(\lambda)$ ratio however indicates that monodomain NCs still contribute quite efficiently to the Raman spectra in the red, in spite of their low extinction cross-section. Furthermore, let us mention again that the amount of monodomain NCs is estimated by TEM analysis to not exceed 30% of the full NCs population in the studied samples. The persistence of the signal from monodomain NCs suggests therefore their strong capacity for light scattering probably originating from their highly efficient plasmon−vibration coupling.

LFRS Measurement from a Population of Au MTPs and Polycrystalline Particles. In addition to the above results obtained from samples in which both polycrystalline and monodomain NCs coexist, the LFRS spectrum measured from a population of Au NCs essentially composed of MTPs and polycrystalline NCs is shown for comparison in Figure 5a. These latter NCs have been synthesized by using a modified Brust's protocol,[30] (see the Supporting Information for more details).

It is straightforward to note that the spectrum measured from this sample does not exhibit such a band splitting as the one observed in Figures 3 and 4. Indeed, only one single low-frequency band due to the quadrupolar vibrational modes of Au NCs is observed. By TEM analysis, it is confirmed that only a weak proportion of monodomain NCs is present in this sample, as illustrated by the TEM image depicted in Figure 5b. Besides, the histogram plotted in Figure 5c indicates that the NCs size dispersion characterizing this last sample is broader than that of the other samples (see Figure S1 in the Supporting Information) but still remains quite narrow with a polydispersity not exceeding 14%. Consequently, only a slight broadening of the Raman bands is expected relative to that of the other samples with a narrower NCs size dispersion. The observation of one single band in the LFRS spectrum plotted in Figure 5a, with no well-resolved substructure discernible from the band profile, can be accurately attributed to the small amount of monodomain NCs whose contribution to the signal is here negligible comparatively to that of the polycrystalline NCs. This last result obtained from a

population containing a weak proportion of monodomain NCs gives further argument in demonstrating the high sensitivity of the LFRS by Au NCs on their crystallinity.

CONCLUSIONS

Polycrystalline and monodomain Au NCs with a few nanometers in diameter and narrow size dispersion have been unselectively synthesized using an organometallic route. Using plasmon mediated low-frequency Raman scattering, the effect of elastic anisotropy on the acoustic vibrations of monodomain NCs is clearly revealed through the splitting of the quadrupolar band, in agreement with resonant ultrasound calculations. Conversely, no splitting is observable in the LFRS spectrum of a sample mainly composed of Au MTPs and polycrystalline NCs. Besides, the excitation wavelength dependence of the measured Raman signal is consistent with the selective contribution of NCs with different crystallinities and related morphologies upon their excitation *via* plasmon−vibration coupling.

A more quantitative analysis of such an excitation wavelength dependence of Raman scattering would require precise information, which is currently still lacking, both on the amounts of NCs related to each crystalline structure and morphology and on the assessment
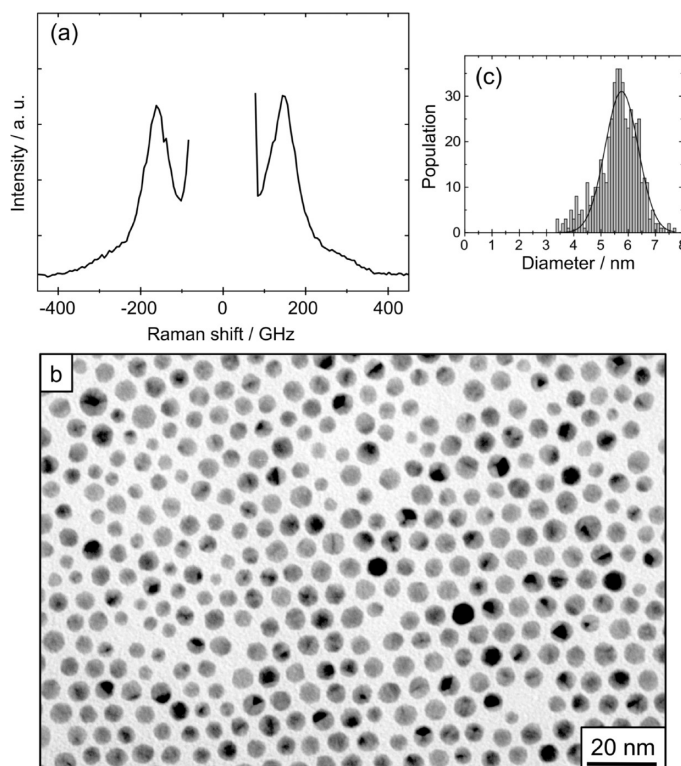

Figure 5. (a) Stokes/anti-Stokes LFRS spectrum measured from a sample mostly composed of Au MTPs and polycrystalline particles using an excitation wavelength of 647.1 nm. (b) TEM image of Au NCs originating from the same colloidal solution. (c) Size distribution histogram of the NCs determined by TEM analysis and the corresponding Gaussian fitting curve (D_{max} = 5.8 nm and σ = 0.75 nm).

of their respective scattering efficiency *via* plasmon−vibration coupling. All the qualitative arguments presented above nevertheless permit a confi-

dent interpretation of the reported observations and bring interesting new insights into the relevance of elastic anisotropy in nanosized crystals.

EXPERIMENTAL METHODS

Synthesis of Both Monodomain and Polycrystalline Au NCs. Au NCs are synthesized by using an organometallic route consisting of a modified Stucky's protocol.[22] Briefly, 0.25 mmol of chlorotriphenylphosphine gold(I) (Strem, 98%) is dissolved in 25 mL of toluene (Riedel-deHaën, >99.5%) and 500 μL of 1-dodecanethiol (Aldrich, ≥98%) is added. In parallel, a second solution is prepared by dissolving 5 mmol of *tert*-butylamine borane complex (Strem, >97%) in 2 mL of toluene. Each solution is stirred in a silicone bath at 100 °C to ensure the total dissolution of all solid products. After having reached the bath temperature, the two solutions are then mixed together. The color of the mixture turns from brown to dark red indicating the NC growth. After 5 min the solution is removed from the bath and progressively cooled to room temperature. At the end of reduction, the NCs are washed with ethanol to eliminate byproduct and are redispersed in neat toluene. The samples are prepared by evaporating overnight a volume of 100 μL of the washed colloidal solution at 10^{-2} M in a glass beaker at the bottom of which a highly oriented pyrolitic graphite (HOPG) substrate is placed. The resulted sample to be studied stands as an assembly of dodecanethiol coated Au NCs deposited on the HOPG substrate.

TEM Characterization. Bright field and conical dark field scan transmission electron microscopy (TEM) analysis of Au NCs is performed by using a JEOL 2010 (200 kV) microscope. To image the NCs, these latter are redispersed in toluene and the obtained colloidal solution is drop cast onto a carbon-coated copper grid (200 mesh).

Extinction Analysis by Spectrophotometric Measurements and DDA Simulations. The extinction spectrum of the Au colloidal solution is measured with a Varian Cary 5000 UV−vis−NIR spectrophotometer. All the calculations of the extinction spectra presented in this paper are carried out using the discrete dipole approximation (DDA) method. This approach is based on the theory originally developed by Purcell and Pennypacker[31] for the study of interstellar dust grains and which has then benefited from some improvements.[32,33] This makes it possible to use the DDA for computing[34] the absorption, extinction, and scattering cross sections of either individual or multiple objects of any size and shape. Besides, this method allows a modeling of systems composed of several materials by means of the appropriate dielectric functions. Here, to simulate the extinction spectra of Au NCs whose size does not exceed a few nanometers, a size-correction of the bulk Au dielectric function has been applied according to the same procedure already presented elsewhere.[35,36] Indeed, this correction aims to account for the finite size effects that affect the dielectric properties of such nanosized metal particles. The volume of the different particles simulated in this work remains constant whatever the particle shape is, and is fixed to match the volume of a sphere of 5 nm in diameter.

LFRS Measurements and Calculation of the Vibrational Frequencies. For the LFRS experiments, the scattered light was dispersed with a Dilor Z40 five-grating monochromator and detected at 90° from the incident light beam by a photomultiplier equipped with a GaAs photocathode. Three different lines of either an Ar⁺ or a Kr⁺ laser are used as the excitation source with the following wavelengths: 514.5, 647.1, and 676.4 nm. It should be noted that the LFRS spectra have been checked to be reproducible at different points of the sample for each excitation wavelength. The high-resolution low-frequency Raman spectrum presented in this work has been recorded by using the green line at 532 nm of a continuous yttrium aluminum garnet (YAG) laser for the excitation of the sample and a six-pass tandem Fabry−Pérot interferometer[37] coupled with a Si avalanche photodiode for the detection of the scattered light.

To facilitate and support our interpretation of the LFRS spectra, the measured frequencies are compared with computational

ones whose calculation is based on the above-mentioned RUS approach.[20] As shown from previous works,[18,19] this method is very useful and relevant for studying the acoustic vibrations of nanoparticles with anisotropic elasticity.

Supporting Information Available: TEM images, size distributions and LFRS spectra of different samples containing a mixture of both polycrystalline and monodomain Au NCs. Protocol for the preparation of the Au colloidal solution which mainly contains MTPs and polycrystalline particles. This material is available free of charge *via* the Internet at http://pubs.acs.org.

REFERENCES AND NOTES

1. Lee, K. S.; El-Sayed, M. A. Gold and Silver Nanoparticles in Sensing and Imaging: Sensitivity of Plasmon Response to Size, Shape, and Metal Composition. *J. Phys. Chem. B* **2006**, *110*, 19220–19225.
2. Kelly, K. L.; Coronado, E.; Zhao, L. L.; Schatz, G. C. The Optical Properties of Metal Nanoparticles: The Influence of Size, Shape, and Dielectric Environment. *J. Phys. Chem. B* **2003**, *107*, 668–677.
3. Noguez, C. Surface Plasmons on Metal Nanoparticles: The Influence of Shape and Physical Environment. *J. Phys. Chem. C* **2007**, *111*, 3806–3819.
4. Weitz, D. A.; Gramila, T. J.; Genack, A. Z.; Gersten, J. I. Anomalous Low-Frequency Raman-Scattering from Rough Metal-Surfaces and the Origin of Surface-Enhanced Raman-Scattering. *Phys. Rev. Lett.* **1980**, *45*, 355–358.
5. Willets, K. A.; Van Duyne, R. P. Localized Surface Plasmon Resonance Spectroscopy and Sensing. *Annu. Rev. Phys. Chem.* **2007**, *58*, 267–297.
6. Huang, W. Y.; Qian, W.; El-Sayed, M. A.; Ding, Y.; Wang, Z. L. Effect of the Lattice Crystallinity on the Electron-Phonon Relaxation Rates in Gold Nanoparticles. *J. Phys. Chem. C* **2007**, *111*, 10751–10757.
7. Tang, Y.; Ouyang, M. Tailoring Properties and Functionalities of Metal Nanoparticles through Crystallinity Engineering. *Nat. Mater.* **2007**, *6*, 754–759.
8. Gu, Q. F.; Krauss, G.; Steurer, W.; Gramm, F.; Cervellino, A. Unexpected High Stiffness of Ag and Au Nanoparticles. *Phys. Rev. Lett.* **2008**, *100*, 045502.
9. Hartland, G. V. Nanoparticle Crystallinity—Is Perfect Better? *Nat. Mater.* **2007**, *6*, 716–718.
10. Lamb, H. On the Vibrations of an Elastic Sphere. *Proc. London Math. Soc.* **1882**, *13*, 189–212.
11. Duval, E.; Boukenter, A.; Champagnon, B. Vibration Eigenmodes and Size of Microcrystallites in Glass—Observation by Very-Low-Frequency Raman-Scattering. *Phys. Rev. Lett.* **1986**, *56*, 2052–2055.
12. Del Fatti, N.; Voisin, C.; Chevy, F.; Vallee, F.; Flytzanis, C. Coherent Acoustic Mode Oscillation and Damping in Silver Nanoparticles. *J. Chem. Phys.* **1999**, *110*, 11484–11487.
13. Hodak, J. H.; Henglein, A.; Hartland, G. V. Coherent Excitation of Acoustic Breathing Modes in Bimetallic Core−Shell Nanoparticles. *J. Phys. Chem. B* **2000**, *104*, 5053–5055.
14. Bachelier, G.; Mlayah, A. Surface Plasmon Mediated Raman Scattering in Metal Nanoparticles. *Phys. Rev. B* **2004**, *69*, 205408.

15. Duval, E. Far-Infrared and Raman Vibrational Transitions of a Solid Sphere:Selection Rules. *Phys. Rev. B* **1992**, *46*, 5795–5797.

16. Hovel, H.; Fritz, S.; Hilger, A.; Kreibig, U.; Vollmer, M. Width of Cluster Plasmon Resonances—Bulk Dielectric Functions and Chemical Interface Damping. *Phys. Rev. B* **1993**, *48*, 18178–18188.

17. Stephanidis, B.; Adichtchev, S.; Etienne, S.; Migot, S.; Duval, E.; Mermet, A. Vibrations of Nanoparticles: From Nanospheres to FCC Cuboctahedra. *Phys. Rev. B* **2007**, *76*, 121404.

18. Portales, H.; Goubet, N.; Saviot, L.; Adichtchev, S.; Murray, D. B.; Mermet, A.; Duval, E.; Pileni, M. P. Probing Atomic Ordering and Multiple Twinning in Metal Nanocrystals through Their Vibrations. *Proc. Natl. Acad. Sci. U.S.A.* **2008**, *105*, 14784–14789.

19. Saviot, L.; Murray, D. B. Acoustic Vibrations of Anisotropic Nanoparticles. *Phys. Rev. B* **2009**, *79*, 214101.

20. Visscher, W. M.; Migliori, A.; Bell, T. M.; Reinert, R. A. On the Normal Modes of Free Vibration of Inhomogeneous and Anisotropic Elastic Objects. *J. Acoust. Soc. Am.* **1991**, *90*, 2154–2162.

21. Crut, A.; Maioli, P.; Del Fatti, N.; Vallee, F. Anisotropy Effects on the Time-Resolved Spectroscopy of the Acoustic Vibrations of Nanoobjects. *Phys. Chem. Chem. Phys.* **2009**, *11*, 5882–5888.

22. Zheng, N.; Fan, J.; Stucky, G. D. One-Step One-Phase Synthesis of Monodisperse Noble-Metallic Nanoparticles and Their Colloidal Crystals. *J. Am. Chem. Soc.* **2006**, *128*, 6550–6551.

23. Ino, S.; Ogawa, S. Multiply Twinned Particles at Earlier Stages of Gold Film Formation on Alkalihalide Crystals. *J. Phys. Soc. Jpn.* **1967**, *22*, 1365–1374.

24. Wang, Z. L. Transmission Electron Microscopy of Shape-Controlled Nanocrystals and Their Assemblies. *J. Phys. Chem. B* **2000**, *104*, 1153–1175.

25. Rodriguez-Fernandez, J.; Novo, C.; Myroshnychenko, V.; Funston, A. M.; Sanchez-Iglesias, A.; Pastoriza-Santos, I.; Perez-Juste, J.; de Abajo, F. J. G.; Liz-Marzan, L. M.; Mulvaney, P. Spectroscopy, Imaging, and Modeling of Individual Gold Decahedra. *J. Phys. Chem. C* **2009**, *113*, 18623–18631.

26. Palpant, B.; Portales, H.; Saviot, L.; Lerme, J.; Prevel, B.; Pellarin, M.; Duval, E.; Perez, A.; Broyer, M. Quadrupolar Vibrational Mode of Silver Clusters from Plasmon-Assisted Raman Scattering. *Phys. Rev. B* **1999**, *60*, 17107–17111.

27. Bachelier, G.; Margueritat, J.; Mlayah, A.; Gonzalo, J.; Afonso, C. N. Size Dispersion Effects on the Low-Frequency Raman Scattering of Quasispherical Silver Nanoparticles: Experiment and Theory. *Phys. Rev. B* **2007**, *76*, 235419.

28. Duval, E.; Portales, H.; Saviot, L.; Fujii, M.; Sumitomo, K.; Hayashi, S. Spatial Coherence Effect on the Low-Frequency Raman Scattering from Metallic Nanoclusters. *Phys. Rev. B* **2001**, *63*, 075405.

29. Portales, H.; Saviot, L.; Duval, E.; Gaudry, M.; Cottancin, E.; Lerme, J.; Pellarin, M.; Broyer, M.; Prevel, B.; Treilleux, M. Resonance and Composition Effects on the Raman Scattering from Silver-Gold Alloy Clusters. *Eur. Phys. J. D* **2001**, *16*, 197–200.

30. Goubet, N.; Ding, Y.; Brust, M.; Wang, Z. L.; Pileni, M. P. A Way To Control the Gold Nanocrystals Size: Using Seeds with Different Sizes and Subjecting Them to Mild Annealing. *ACS Nano* **2009**, *3*, 3622–3628.

31. Purcell, E. M.; Pennypacker, C. R. Scattering and Absorption of Light by Nonspherical Dielectric Grains. *Astrophys. J.* **1973**, *186*, 705–714.

32. Goodman, J. J.; Draine, B. T.; Flatau, P. J. Application of Fast-Fourier-Transform Techniques to the Discrete-Dipole Approximation. *Opt. Lett.* **1991**, *16*, 1198–1200.

33. Draine, B. T.; Flatau, P. J. Discrete-Dipole Approximation for Scattering Calculations. *J. Opt. Soc. Am. A* **1994**, *11*, 1491–1499.

34. Draine, B. T.; Flatau, P. J. *Program DDSCAT 7.0*; University of California; CA Scripps Institution of Oceanography: San Diego, La Jolla, CA, 2008.

35. Coronado, E. A.; Schatz, G. C. Surface Plasmon Broadening for Arbitrary Shape Nanoparticles: A Geometrical Probability Approach. *J. Chem. Phys.* **2003**, *119*, 3926–3934.

36. Portales, H.; Pinna, N.; Pileni, M. P. Optical Response of Ultrafine Spherical Silver Nanoparticles Arranged in Hexagonal Planar Arrays Studied by the DDA Method. *J. Phys. Chem. A* **2009**, *113*, 4094–4099.

37. Lindsay, S. M.; Anderson, M. W.; Sandercock, J. R. Construction and Alignment of a High-Performance Multipass Vernier Tandem Fabry−Pérot Interferometer. *Rev. Sci. Instrum.* **1981**, *52*, 1478–1486.

ARTICLE